

Electrosynthesis

International Edition: DOI: 10.1002/anie.201903936
German Edition: DOI: 10.1002/ange.201903936

Paired Electrocatalytic Oxygenation and Hydrogenation of Organic Substrates with Water as the Oxygen and Hydrogen Source

Peili Zhang, Xia Sheng, Xiaoyu Chen, Zhiyong Fang, Jian Jiang, Mei Wang, Fusheng Li, Lizhou Fan, Yansong Ren, Biaobiao Zhang, Brian J. J. Timmer, Mårten S. G. Ahlquist, and Licheng Sun*

Abstract: The use of water as an oxygen and hydrogen source for the paired oxygenation and hydrogenation of organic substrates to produce valuable chemicals is of utmost importance as a means of establishing green chemical syntheses. Inspired by the active Ni^{3+} intermediates involved in electrocatalytic water oxidation by nickel-based materials, we prepared NiB_x as a catalyst and used water as the oxygen source for the oxygenation of various organic compounds. NiB_x was further employed as both an anode and a cathode in a paired electrosynthesis cell for the respective oxygenation and hydrogenation of organic compounds, with water as both the oxygen and hydrogen source. Conversion efficiency and selectivity of $\geq 99\%$ were observed during the oxygenation of 5-hydroxymethylfurfural to 2,5-furandicarboxylic acid and the simultaneous hydrogenation of *p*-nitrophenol to *p*-aminophenol. This paired electrosynthesis cell has also been coupled to a solar cell as a stand-alone reactor in response to sunlight.

Water is an abundant resource on earth and is widely used as either an oxygen or a hydrogen source during naturally occurring biosynthetic oxygenation and hydrogenation reactions.^[1,2] Inspired by natural systems, we consider water to represent an ideal source of oxygen and hydrogen instead of

high-cost H_2 or chemical oxidants/reductants for catalytic oxygenation and hydrogenation in green chemical processes.

During the last decade, the electrocatalytic oxygenation of organic compounds to value-added products with water as the oxygen source has started to attract increased attention. Several interesting electrocatalytic systems have been reported with improving performance. Ni_2P ,^[3a] Co-P ,^[3b] Ni_3S_2 ,^[3c] Ni_xB ,^[3d] NiFe LDH ,^[3e] and noble metals (Au and Pd) and their alloys^[3f] are used as efficient electrocatalysts for the oxidation of furanics and other biomass-derived platform chemicals. Recently, the Schuhmann group provided new insight into the oxidation pathway of 5-hydroxymethylfurfural (HMF) through operando electrochemistry-coupled attenuated total reflection infrared spectroscopy with Ni_xB as the catalyst.^[3d] To date, the majority of reports have focused on conversion efficiency and selectivity, whereas the water-active process, the catalytic active sites, and the oxygen-atom-transfer mechanism remain ambiguous.^[3]

In electrocatalytic oxygenation reactions, protons are generated as a by-product.^[4] Recently, these reactions have been paired with the electrocatalytic hydrogen evolution reaction (HER) to increase the energy-conversion efficiency.^[3] However, as compared with HER, organic oxygenation reactions are kinetically sluggish, especially in the late stages of the reaction, owing to the decrease in reactant concentrations. Thus, both catalytic efficiency and electron economy could be improved by pairing organic oxygenation with a rate-matched organic hydrogenation to create sustainable chemical-synthesis strategies.^[4]

In this study, the electrocatalytic oxygen-atom-transfer mechanism was investigated in 1M KOH with NiB_x ($x = 0.40 \pm 0.05$) as the catalyst and the oxygenation of HMF to 2,5-furandicarboxylic acid (FDCA) as a model reaction. Experiment results indicated that the electrogenerated Ni^{3+} species are the active intermediates. Furthermore, a paired electrolysis system was constructed by combining the electrocatalytic oxygenation of HMF to FDCA and the hydrogenation of *p*-nitrophenol (*p*-NP) to *p*-aminophenol (*p*-AP). Conversion, efficiency, selectivity, and faradic efficiency as high as $\geq 99\%$ were attained on both sides with water as the oxygen and hydrogen source. This paired electrolyzer uses electricity to drive the organic oxygenation and hydrogenation reactions in aqueous solutions, without the need to handle hazardous gaseous hydrogen or oxygen or to incorporate external oxidants/reductants.

The NiB_x working electrode (WE) was prepared by electroless plating for 2 h with a nickel foam (NF) substrate at 90 °C in NaOH aqueous solutions (pH 13.5) containing

[*] Dr. P. Zhang, Dr. X. Sheng, L. Fan, Dr. Y. Ren, Dr. B. Zhang, Dr. B. J. J. Timmer, Prof. L. Sun
Department of Chemistry, School of Engineering Sciences in Chemistry, Biotechnology and Health
KTH Royal Institute of Technology
10044 Stockholm (Sweden)
E-mail: lichengs@kth.se

Dr. P. Zhang, Z. Fang, J. Jiang, Prof. M. Wang, Dr. F. Li, Prof. L. Sun
State Key Laboratory of Fine Chemicals, Institute of Artificial Photosynthesis, DUT-KTH Joint Education and Research Centre on Molecular Devices, Dalian University of Technology
116024 Dalian (China)

X. Chen, Dr. M. S. G. Ahlquist
Department of Theoretical Chemistry and Biology, School of Engineering Sciences in Chemistry, Biotechnology and Health
KTH Royal Institute of Technology
10691 Stockholm (Sweden)

Supporting information and the ORCID identification number(s) for the author(s) of this article can be found under:
<https://doi.org/10.1002/anie.201903936>.

© 2019 The Authors. Published by Wiley-VCH Verlag GmbH & Co. KGaA. This is an open access article under the terms of the Creative Commons Attribution Non-Commercial NoDerivs License, which permits use and distribution in any medium, provided the original work is properly cited, the use is non-commercial and no modifications or adaptations are made.

Ni(Cl)₂·6H₂O (125 mM), ethanediamine (750 mM), and NaBH₄ (55 mM).^[5] The Ni:B atomic ratio (1:0.40 ± 0.05) was verified by inductively coupled plasma optical emission spectroscopy, and the NiB_x loading on the NF surface was (2.47 ± 0.10) mg cm⁻². Top-view scanning electron microscopy (SEM) images showed that NiB_x was uniformly deposited on the NF to provide a rough surface (Figure 1 a,b). High-

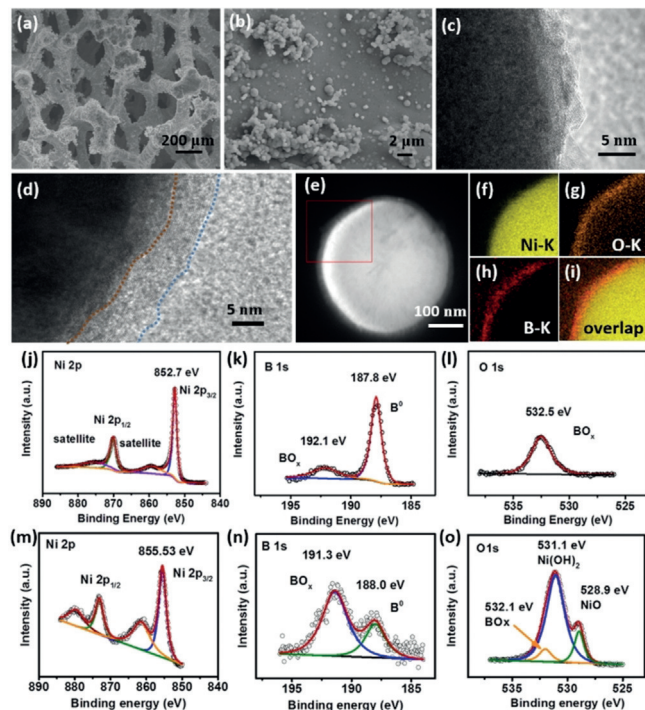


Figure 1. a,b) SEM images and c) TEM image of the as-prepared NiB_x@NF; d) TEM image and e–i) elemental mapping of NiB_x@NF after controlled potential electrolysis at 0.50 V versus SHE; j–l) high-resolution Ni 2p (j), B 1s (k), and O 1s XPS spectra (l) obtained for the as-prepared NiB_x@NF; m–o) high-resolution Ni 2p (m), B 1s (n), and O 1s XPS spectra (o) obtained for NiB_x@NF after controlled potential electrolysis at 0.50 V versus SHE.

resolution transmission electron microscopy (TEM) images (Figure 1 c) suggested that the surface particles were composed of amorphous nickel boride and nickel. X-ray photoelectron spectroscopy (XPS) analysis confirmed that Ni and B were the main components (see Figure S1 in the Supporting Information). The Ni 2p_{3/2} peak at 852.7 eV can be assigned to Ni⁰, while the B 1s peak at 187.8 eV can be assigned to B⁰, as expected for nickel borides.^[6] The weak B 1s hump at 192.1 eV and the O 1s peak at 532.5 eV are due to small amounts of boron oxide (Figure 1 j–l).^[6b]

Linear sweep voltammetry (LSV) and in situ Raman spectroscopy were used to study the formation of the Ni³⁺ species. The LSV sweep of NiB_x@NF in 1 M KOH showed an oxidation peak corresponding to the Ni²⁺/Ni³⁺ oxidation at 0.50 V versus the standard hydrogen electrode (SHE); see Figure S2). After electrolysis at 0.50 V versus SHE, the surface of the NiB_x@NF was analyzed by TEM (Figure 1 d–i) and XPS (Figure 1 m–o). TEM images and TEM mapping demonstrated that a new shell was generated on the surface of

the NiB_x particles (Figures 1 d,i), while Ni 2p_{3/2}, O 1s and B 1s XPS data indicated that this shell was composed of a mixture of Ni oxide and Ni hydroxide (Figure 1 m–o). Raman spectra of the NiB_x@NF at 0.50 V versus SHE showed the emergence of a Ni³⁺–O bending peak at 471 cm⁻¹ and a Ni³⁺–O stretching peak at 554 cm⁻¹, thus demonstrating that NiOOH (Ni³⁺) was the electrogenerated intermediate (Figure 2 a).^[7]

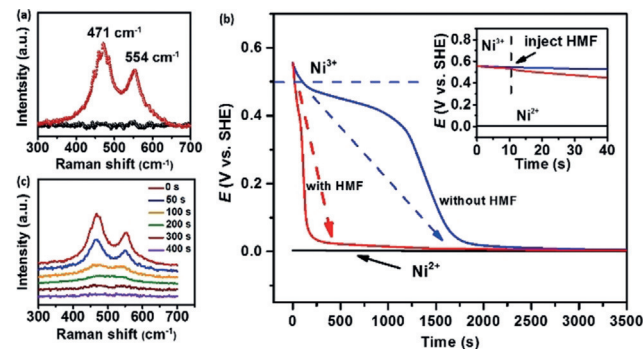


Figure 2. a) Raman spectra of NiB_x@NF at 0.50 V versus SHE in 1 M KOH (red) and the as-prepared NiB_x@NF (black); b) graph of open-circuit potential versus time to investigate the lifetime of the electrogenerated Ni³⁺ species on the surface of NiB_x@NF in 1 M KOH with (red curve) and without HMF (blue curve); c) change in the Raman spectrum of NiB_x@NF after the injection of HMF into the electrolyte.

Initially, the oxidizability of Ni³⁺ for HMF oxygenation was computationally and experimentally investigated. The oxygenation of HMF to FDCA is a three-step process and includes the oxidation of the hydroxy and aldehyde groups to carboxylic acids (see Figure S3).^[8] The oxidation of HMF to FDCA can proceed through two pathways, distinguished by the primary oxidation of the hydroxy or carbonyl functionality (see Figure S3 a). The standard potential (E°) for each step on both pathways was estimated by DFT calculations (see Figure S3 b). HMF is converted into 5-hydroxymethyl-2-furancarboxylic acid (HMFA) with an E° value of 0.098 V versus SHE, whereas the competitive reaction from HMF to the dialdehyde 2,5-diformylfuran (DFF) has an E° value of -0.187 V versus SHE. Further oxidation of DFF and HMFA leads to the formation of 5-formyl-2-furancarboxylic acid (FFCA) with E° values of 0.119 and -0.167 V versus SHE, respectively. The final oxidation of FFCA to FDCA occurs at an E° value of 0.109 V versus SHE. The reduction potential of Ni³⁺/Ni²⁺ is approximately 0.50 V versus SHE.^[9] Therefore, based on the DFT calculations, the oxidizing ability of Ni³⁺ would be expected to drive each step during the oxidation of HMF to FDCA. Indeed, chemical oxygenation of HMF with the Ni³⁺ complex Ni₃O₂(OH)₄^[10] (see Figure S4) showed a high yield ($\geq 99\%$) of FDAC in aqueous media. The powder X-ray diffraction (XRD) pattern of the Ni material after oxygenation demonstrated the formation of Ni(OH)₂, which is indicative of the Ni³⁺ to Ni²⁺ redox process responsible for the oxidation (see Figure S4).

The activity of electrochemically generated Ni³⁺ toward the oxygenation of HMF in 1 M KOH was further verified by an open-circuit potential versus time (OCPT) experiment. The change in the E_{OCP} value reflects variations in the WE

surface that, in turn, depend on changes in the active species at the electrode–solution interface.^[11] In this study, E_{OCP} is associated with the anodic reaction occurring at the WE surface. The electrochemically generated Ni^{3+} species corresponds to an E_{OCP} value of 0.50 V versus SHE, whereas the Ni^{2+} species corresponds to an E_{OCP} value of -0.01 V versus SHE. The surface Ni was oxidized to Ni^{3+} at 0.50 V versus SHE ($\text{Ni}(\text{OH})_2 + \text{OH}^- \rightarrow \text{NiOOH} + \text{H}_2\text{O} + \text{e}^-$), followed by a spontaneous transition to Ni^{2+} ($\text{NiOOH} + \text{H}_2\text{O} + \text{e}^- \rightarrow \text{Ni}(\text{OH})_2 + \text{OH}^-$) with a lifetime of 1700 s (Figure 2b). A control OCPT experiment showed that the lifetime of the electrochemically generated Ni^{3+} was shortened to 200 s upon the addition of HMF to the electrolyte (Figures 2b,c). This accelerated quenching indicates that the electrochemically generated Ni^{3+} is the active intermediate during the oxygenation of HMF.

The effect of water on the catalytic oxygenation of HMF with $\text{NiB}_x@/\text{NF}$ was assessed by performing trials in acetonitrile (see Figure S5). The blank cyclic voltammogram (CV) curve obtained with $\text{NiB}_x@/\text{NF}$ in acetonitrile showed a Faradaic silent curve before 2.2 V versus SHE, thus indicating difficulty in forming the Ni^{3+} species without water. The subsequent addition of HMF gave an identical curve to that produced during the blank CV, indicating that HMF oxygenation did not proceed without the Ni^{3+} species. A control experiment with $\text{NiB}_x@/\text{NF}$ in acetonitrile with water produced a water oxidation current at 1.90 V versus SHE, thus demonstrating the formation of Ni^{3+} . When water was added together with HMF, a current increase observed at 1.70 V versus SHE was assigned to the oxygenation of HMF. These results show that HMF was oxygenated, with water serving as the oxygen source, and that Ni^{3+} is an essential intermediate.

We concluded that the electrocatalytic oxygenation of HMF with $\text{NiB}_x@/\text{NF}$ as the WE and water as an oxygen source occurs through a two-step oxygen-transfer mechanism (see Figure S6). First, Ni^{2+} is electrooxidized to Ni^{3+} with a newly bonded OH^- group originating from water. The resulting Ni^{3+} species reacts with HMF, DFF, and/or HMFA to produce FDCA, along with the regeneration of Ni^{2+} . In this process, water is the only oxygen source.

The electrocatalytic performance of $\text{NiB}_x@/\text{NF}$ toward HMF oxygenation in 1 M KOH is summarized in Figure 3. The LSV curve of $\text{NiB}_x@/\text{NF}$ without HMF shows a $\text{Ni}^{2+}/\text{Ni}^{3+}$ oxidation peak at 0.50 V versus SHE, followed by a silent region between 0.55 and 0.75 V versus SHE, and the OER beyond 0.75 V versus SHE.^[12] To investigate the extent to which oxygenation was catalyzed, 10 mM HMF was added to the electrolyte. The LSV curve shows a similar $\text{Ni}^{2+}/\text{Ni}^{3+}$ process at 0.50 V versus SHE, followed by a significant enhancement at 0.60 V versus SHE with a peak current density of 40 mA cm^{-2} , which is attributed to the HMF oxygenation reaction (Figure 3a). It is evident that HMF oxygenation is favored over the OER. Furthermore, the current density beyond 0.70 V versus SHE is attributed to the superposition of HMF oxygenation and the OER. Control experiments with a glassy carbon plate produced a Faradaic silent region from 0.20 to 0.80 V versus SHE both with and without the HMF (Figure 3b). These results indicate that $\text{NiB}_x@/\text{NF}$ promoted HMF oxygenation through a electro-

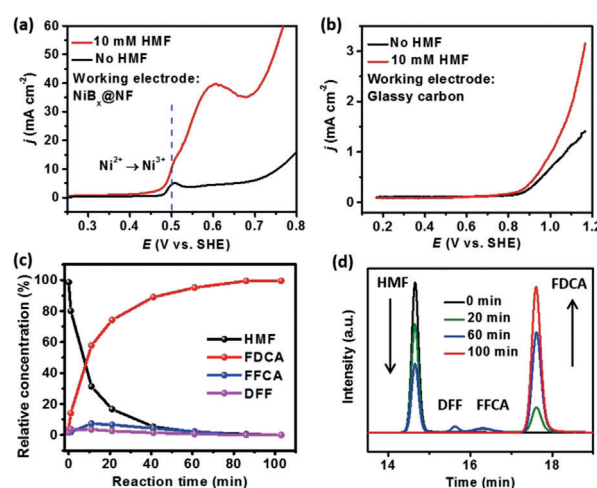


Figure 3. a) LSV curves for $\text{NiB}_x@/\text{NF}$ in 1 M KOH with and without HMF (10 mM); b) LSV curves for a glassy carbon plate in 1 M KOH with and without 10 mM HMF (scan rate, 5 mVs^{-1}); c) concentration of HMF, FDCA, and intermediates versus electrolysis time; d) HPLC chromatograms acquired at various electrolysis times.

catalytic process. Further research showed that the peak current densities at 0.60 V versus SHE increased linearly along with increases in the HMF concentration (see Figure S7). These results suggest that the oxygenation on the WE surface is a diffusion-controlled process.

Conversion, selectivity, and Faradaic efficiency were investigated during the oxygenation of HMF to FDCA by chronoamperometry. A constant potential of 0.60 V versus SHE was applied during the electrolysis (Figure 3c,d). The reaction process was monitored by high performance liquid chromatography (HPLC). The results showed that $(99.8 \pm 0.2)\%$ of the HMF had been converted into FDCA after 100 min. DFF and FFCA were identified by HPLC as intermediates. Overall, the oxygenation of HMF to FDCA is a six-electron process,^[3d,8] and the Faradaic efficiency of the electrocatalytic HMF oxygenation was approximately $(99.5 \pm 0.5)\%$, as based on the electrolysis and the theoretical charges for the formation of FDCA (see Figure S8).

To enhance atom utilization, a cathodic reaction is necessary to consume the protons generated during the oxygenation of HMF. The hydrogenation of nitro compounds to their corresponding amines is important for the synthesis of fine chemicals, such as dyes and pigments.^[13] In subsequent trials, the hydrogenation of *p*-NP to *p*-AP was used as a model reaction in conjunction with $\text{NiB}_x@/\text{NF}$ as the WE and water as the hydrogen source.

The electrocatalytic hydrogenation of *p*-NP proceeds through three two-electron–two-proton processes (see Figure S9). Under standard conditions, the ΔG value was found to be negative ($\Delta G < 0$) for each step, thus indicating that the hydrogenation of *p*-NP is an exergonic process. The reduction potentials for the continuous reduction reactions are 0.603, 0.333, and 0.719 V versus SHE ($\text{R}^2\text{NO}_2 + 2\text{H}^+ + 2\text{e}^- \rightarrow \text{R}^2\text{NO} + \text{H}_2\text{O}$, $\text{R}^2\text{NO} + 2\text{H}^+ + 2\text{e}^- \rightarrow \text{R}^2\text{NHOH}$, $\text{R}^2\text{NHOH} \rightarrow \text{R}^2\text{NH} + \text{H}_2\text{O}$, $\text{R}^2\text{NH} + 2\text{H}^+ + 2\text{e}^- \rightarrow \text{R}^2\text{NH}_2$, $\text{R}^2\text{NO}_2 = p$ -nitrophenol) and thus occur prior to hydrogen evolution on

a thermodynamic basis. These calculations demonstrate that the reduction of nitrosamine to hydroxylamine requires the highest potential of 0.333 V versus SHE.

In 1 M KOH, NiB_x@NF showed an onset potential of -0.90 V versus SHE for HER (Figure 4a). After the addition of *p*-NP, the LSV curve exhibited an onset potential of -0.60 V vs. SHE, followed by a current density of -40 mA cm⁻² at -0.83 V vs. SHE (0 V vs. RHE). The

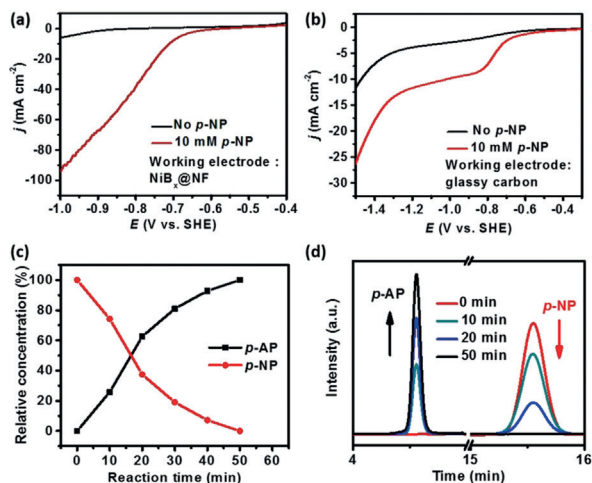


Figure 4. a) LSV curves for NiB_x@NF in 1 M KOH in the absence and presence of 10 mM *p*-NP, at a scan rate of 5 mVs⁻¹; b) polarization curves for a glassy carbon plate in 1 M KOH in the absence and presence of 10 mM *p*-NP, at a scan rate of 5 mVs⁻¹; c) [*p*-NP] and [*p*-AP] versus electrolysis time; d) HPLC chromatograms acquired at various electrolysis time points.

increased current density beyond -0.90 V versus SHE is attributed to the superposition of the hydrogenation reaction and the HER. These results indicate that the targeted nitro-group hydrogenation occurred prior to the HER, and that a high Faradaic efficiency can readily be achieved through controlling the applied potential. Control experiments with a glassy carbon electrode showed a similar activity toward *p*-NP hydrogenation with an onset potential of -0.65 V versus SHE (Figure 4b). It is evident that the hydrogenation of *p*-NP in 1 M KOH proceeds by an electroreduction mechanism.^[14] Furthermore, a linear relationship was observed between the *p*-NP concentration and the corresponding current density (see Figure S10), thus indicating a molecular diffusion reaction process. The catalytic properties of NiB_x@NF during the hydrogenation of *p*-NP were further explored by chronoamperometry. Conversion and selectivity of ≥ 99% were observed after 50 min at the applied potential of -0.83 V versus SHE (Figure 4c,d; see also Figure S11). During the catalytic process, no intermediates were observed by HPLC. A Faradaic efficiency of approximately 99% was calculated by comparing the charge consumed in the production of *p*-AP with the integrated current.

Paired electrolysis combines two desirable half-reactions to maximize energy efficiency and the formation of useful products.^[15] As previously described, the as-prepared NiB_x@NF exhibited promising catalytic performance during

the electrocatalytic oxygenation and hydrogenation half-reactions under the same conditions. Hence, we integrated these two half-reactions in an electrolyzer to realize paired electrolysis, using the full potential of water as both an oxygen and a hydrogen source (Figure 5a). The catalytic activity of

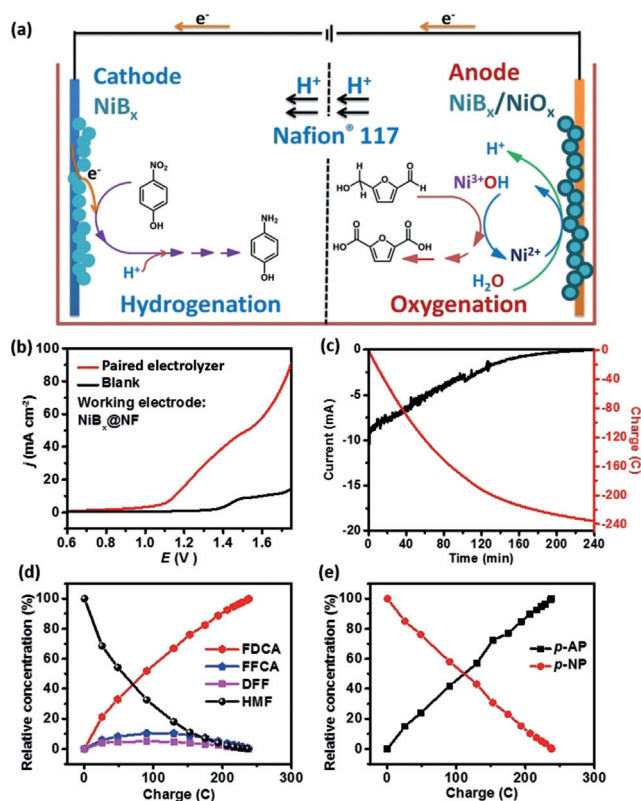


Figure 5. a) Paired electrochemical cell; b) LSV curves for the paired electrolyzer in 1.0 M KOH in the absence and presence of organic reactants (scan rate, 5 mVs⁻¹); c) current–time and charge–time transients during constant-potential electrolysis at 1.40 V; d) results from analysis of the anode side at various charges; e) results from analysis of the cathode side at various charges.

NiB_x@NF during HMF oxygenation and *p*-NP hydrogenation in the paired electrolyzer was further evaluated by acquiring polarization curves and electrolysis (Figure 5). In the absence of HMF and *p*-NP, NiB_x@NF exhibited HER activity beyond 1.65 V (Figure 5b). The LSV curve obtained during the paired oxygenation of HMF and hydrogenation of *p*-NP (Figure 5b) exhibited an onset potential of 1.10 V and reached a plateau of 50 mA cm⁻² at 1.5 V. These results indicate that the paired reactions proceeded preferentially, rather than hydrogen evolution.

An applied potential of 1.40 V was used for further chronoamperometric tests. In the electrolysis process, the Faradaic current density gradually decreased to 0 within 240 min, with a charge buildup of 238 C (Figure 5c). The starting substrates (HMF and *p*-NP) were consumed with ≥ 99% conversion into the corresponding products (Figures 5d,e). The expected intermediates FFCA and DFF were also detected by HPLC (Figure 5d). Furthermore, a Faradaic efficiency of ≥ 99% was attained for each side.

The design of the paired electrolyzer is scalable to meet different requirements. A simple photoelectrochemically driven oxygenation and hydrogenation device was created by connecting solar cells (1.5 V silicon solar panel) and the paired electrolyzer in series (see Figure S12). This photo-voltaic-integrated electrolyzer demonstrated the simultaneous oxygenation of HMF and hydrogenation of *p*-NP in an aqueous solution under outdoor sunlight with high conversion and selectivity ($\geq 99\%$). High conversion and selectivity were also observed when HMF was replaced with furan-2-carbaldehyde, furan-2-ylmethanol, pyridin-4-ylmethanol, and 4-(hydroxymethyl)phenol as the compounds undergoing oxygenation, and when *p*-NP was replaced with *m*-NP, *o*-NP, 4-nitrobenzotrile, and 1-ethynyl-4-nitrobenzene (see Figures S13 and S14 and Table S1 in the Supporting Information).

In summary, we have developed a paired electrochemical system for the oxygenation and hydrogenation of organic compounds to replace the chemical-driven stoichiometric reactions with sacrificial reagents. Water was found to be essential as the oxygen and hydrogen source for these redox reactions in the paired electrolyzer. The as-designed electrochemical cell exhibited high conversion, selectivity, and Faradaic efficiency at both the anode and cathode simultaneously, without the involvement of oxygen and hydrogen. For example, a conversion efficiency of $\geq 99\%$ was observed for the oxygenation of HMF to FDCA and the hydrogenation of *p*-NP to *p*-AP. The experimental results show that this paired electrolyzer can be extended to other organic substrates. This new (photo)electrocatalytic cell system should have practical applications in future green chemical systems using electricity or sunlight as the energy input and water as both the oxygen and hydrogen sources.

Experimental Section

All electrochemical experiments were performed with a CH Instrument 660E potentiostat. The electrochemical cell contained the sample as a WE, a platinum foil (4 cm²) as an auxiliary electrode, and Hg/HgO (1M KOH, Tjaida) as a reference electrode ($E_{\text{Hg/HgO}}^{\circ} = 0.098$ V vs. SHE). The reference electrode was calibrated by measuring the SHE potential. Potentials were converted to SHE through the Nernst equation: $E_{\text{SHE}} = E_{\text{Hg/HgO}} + 0.059 \text{ pH} + E_{\text{Hg/HgO}}^{\circ}$. The internal resistance between the reference and WE (R_{u}) was determined by the automatic current interrupt technique ($R_{\text{u}} = (0.8 \pm 0.1) \Omega$). *i*R compensation during LSV sweeps was performed using the automatic current interrupt method, with a value of $75\% \times R_{\text{u}}$. Chronopotentiometry measurements were performed under an argon atmosphere (unless stated otherwise) with an H-type cell to evaluate the catalytic activity. Nafion[®] 117 membranes were used to separate the anodic and cathodic compartments.

Acknowledgements

We acknowledge the financial support of this work by the Swedish Energy Agency, the Knut and Alice Wallenberg Foundation (KAW 2016.0072), the Swedish Research Council (2017-00935), the National Basic Research Program of China (973 Program, 2014CB239402), and the Fundamental Research Funds for the Central Universities of China (DUT17RC(3)083).

Conflict of interest

The authors declare no conflict of interest.

Keywords: electrochemistry · green chemical synthesis · hydrogenation · oxygenation · water

How to cite: *Angew. Chem. Int. Ed.* **2019**, *58*, 9155–9159
Angew. Chem. **2019**, *131*, 9253–9257

- [1] D. A. Bryant, N. U. Frigaard, *Trends Microbiol.* **2006**, *14*, 488–496.
- [2] S. G. Sligar, T. M. Makris, I. G. Denisov, *Biochem. Biophys. Res. Commun.* **2005**, *338*, 346–354.
- [3] a) B. You, N. Jiang, X. Liu, Y. Sun, *Angew. Chem. Int. Ed.* **2016**, *55*, 9913–9917; *Angew. Chem.* **2016**, *128*, 10067–10071; b) N. Jiang, B. You, R. Boonstra, I. M. T. Rodriguez, Y. Sun, *ACS Energy Lett.* **2016**, *1*, 386–390; c) B. You, N. Jiang, M. Sheng, M. W. Bhushan, Y. Sun, *ACS Catal.* **2016**, *6*, 714–721; d) S. Barwe, J. Weidner, S. Cychy, D. M. Morales, S. Dieckhöfer, D. Hiltrop, J. Masa, M. Muhler, W. Schuhmann, *Angew. Chem. Int. Ed.* **2018**, *57*, 11460–11464; *Angew. Chem.* **2018**, *130*, 11631–11636; e) W. Liu, L. Dang, Z. Xu, H. Yu, S. Jin, G. W. Huber, *ACS Catal.* **2018**, *8*, 5533–5541; f) D. J. Chadderdon, L. Xin, J. Qi, Y. Qiu, P. Krishna, K. L. More, W. Li, *Green Chem.* **2014**, *16*, 3778–3786.
- [4] a) M. G. Walter, E. L. Warren, J. R. McKone, S. W. Boettcher, Q. Mi, E. A. Santori, N. S. Lewis, *Chem. Rev.* **2010**, *110*, 6446–6473; b) K. Li, Y. Sun, *Chem. Eur. J.* **2018**, *24*, 18258–18270.
- [5] P. Zhang, M. Wang, Y. Yang, T. Yao, H. Han, L. Sun, *Nano Energy* **2016**, *19*, 98–107.
- [6] a) A. P. Grosvenor, M. C. Biesinger, R. St. C. Smart, N. S. McIntyre, *Surf. Sci.* **2006**, *600*, 1771–1779; b) J. Legrand, A. Taleb, S. Gota, M.-J. Guittet, C. Petit, *Langmuir* **2002**, *18*, 4131–4137.
- [7] B. S. Yeo, A. T. Bell, *J. Phys. Chem. C* **2012**, *116*, 8394–8400.
- [8] Z. Zhang, G. W. Huber, *Chem. Soc. Rev.* **2018**, *47*, 1351–1390.
- [9] a) L. Hu, Z. Yu, Z. Hu, Y. Song, F. Zhang, H. Zhu, S. Jiao, *Electrochim. Acta* **2015**, *174*, 273–281; b) M. J. Grill, J. Ogle, A. Stephen, S. A. Miller, *J. Org. Chem.* **2006**, *71*, 9291–9296.
- [10] B. Polteau, F. Tessier, F. Cheviré, L. Cario, F. Odobel, S. Jobic, *Solid State Sci.* **2016**, *54*, 37–42.
- [11] T. Liu, B. E. Conway, *J. Appl. Electrochem.* **1987**, *17*, 983–996.
- [12] J. Jiang, M. Wang, W. Yan, X. Liu, J. Liu, J. Yang, L. Sun, *Nano Energy* **2017**, *38*, 175–184.
- [13] a) A. Goyal, S. Bansal, S. Singhal, *Int. J. Hydrogen Energy* **2014**, *39*, 4895–4908; b) B. Dutta, S. Biswas, V. Sharma, N. O. Savage, S. P. Alpay, S. L. Suib, *Angew. Chem. Int. Ed.* **2016**, *55*, 2171–2175; *Angew. Chem.* **2016**, *128*, 2211–2215; c) D. Iranshahi, E. Pourazadi, A. M. Bahmanpour, M. R. Rahimpour, *Int. J. Hydrogen Energy* **2011**, *36*, 3483–3495.
- [14] a) C. L. Forryan, R. G. Compton, *Phys. Chem. Chem. Phys.* **2003**, *5*, 4226–4230; b) S. Möhle, M. Zirbes, E. Rodrigo, T. Gieshoff, A. Wiebe, S. R. Waldvogel, *Angew. Chem. Int. Ed.* **2018**, *57*, 6018–6041; *Angew. Chem.* **2018**, *130*, 6124–6149.
- [15] a) M. Yan, Y. Kawamata, P. S. Baran, *Chem. Rev.* **2017**, *117*, 13230–13319; b) R. S. herbo, R. S. Delima, V. A. Chiykowski, B. P. MacLeod, C. P. Berlinguette, R. S. Sherbo, *Nat. Catal.* **2018**, *1*, 501–507.

Manuscript received: April 4, 2019

Accepted manuscript online: April 26, 2019

Version of record online: May 22, 2019